Uniform Ordered Two-Dimensional Mesoporous TiO_2 Nanosheets from Hydrothermal-Induced Solvent-Confined Monomicelle Assembly

Kun Lan[a], Yao Liu[a], Wei Zhang[a], Yong Liu[a], Ahmed Elzatahry[b], Ruicong Wang[a], Yongyao Xia[a], Daifallah Al-Dahyan[c], Nanfeng Zheng[d], Dongyuan Zhao[a]*

[a] Department of Chemistry, Shanghai Key Laboratory of Molecular Catalysis and Innovative Materials, Laboratory of Advanced Materials, *i*ChEM (Collaborative Innovation Center of Chemistry for Energy Materials), Fudan University, Shanghai, 200433, P. R. China.

[b] Materials Science and Technology Program, College of Arts and Sciences, Qatar University, PO Box 2713, Doha 2713, Qatar

[c] Department of Chemistry, College of Science, King Saud University, Riyadh 11451, Saudi Arabia

[d] Department of Chemistry, College of Chemistry and Chemical Engineering, Xiamen University, Xiamen, Fujian, 361005, P. R. China

ABSTRACT: Two-dimensional (2D) nanomaterials have been the focus of substantial research interest recently owing to their fascinating and excellent properties. However, 2D porous materials have remained quite rare due to the difficulty of creating pores in 2D nanostructures. Here, we have synthesized a novel type of single-layered 2D mesoporous TiO_2 nanosheets with very uniform size and thickness as well as ordered mesostructure from an unprecedented hydrothermal-induced solvent-confined assembly approach. The F127/TiO_2 spherical monomicelles are first formed and redispersed in ethanol and glycerol, followed by a hydrothermal treatment to assemble these subunits into single-layered 2D mesostructure owing to the confinement effect of highly adhered glycerol solvent. The obtained 2D mesoporous TiO_2 nanosheets have a relative mean size at around 500 $\times$ 500 nm and can be randomly stacked into a bulk. The TiO_2 nanosheets possess only one layer of ordered mesopores with a pore size of 4.0 nm, a very high surface area of 210 m^2

g^{-1} and a uniform thickness of 5.5 nm. The thickness can be further manipulated from 5.5 to 27.6 nm *via* simply tuning precursor concentration or solvent ratio. Due to the well-defined 2D morphology and large mesoporosity as well as crystalline anatase mesopore walls, these uniform TiO_2 nanosheets are capable of providing large accessible voids for sodium ion adsorption and intercalation as well as preventing volume expansion. As expected, these mesoporous TiO_2 nanosheets have exhibited an excellent reversible capacity of 220 mAh g^{-1} at 100 mA g^{-1} as sodium-ion battery anodes, and they can retain at 199 mAh g^{-1} after numerous cycles at different current densities. The capacity is retained at 44 mAh g^{-1} even at a large current density of 10 A g^{-1} after 10000 cycles, demonstrating a remarkable performance for energy storage.

INTRODUCTION

Two-dimensional (2D) nanomaterials have been receiving much attention due to their fascinating optical and electrical properties resulting from the reduction of dimensions.[1-18] Construction of 2D porous materials has been an appealing endeavor in materials science over the last few years motivated by the exceptional porous structure in combination with the intrinsic properties of 2D morphologies.[19-22] For instance, the bottom-up approach is an essential method for the fabrication of crystalline 2D conjugated polymers with well-defined micropore structures, which has met less success.[23, 24] The block copolymer lithography approach[25] used to make graphene nanomesh (in-plane pores in graphene) is suitable for scalable production and rational design of graphene-based nanodevices, but the method is limited due to the usage of toxic gas, high cost and low production. While some chemical active agents such as KOH[26] have widely been used for the fabrication of porous carbon materials, the chemical-etching method may introduce considerable defects in the graphene structures. Another several synthetic strategies have been made to fabricate 2D porous nanomaterials such as local oxidation, defects degradation on graphene by utilizing electron beam, photo, and oxygen plasma-etching approaches.[27-29] However, accurate control over the shape, size and distribution of the formed porous structure remains difficult. To date, it is still a large scientific and technological challenge for

creating stable and tunable pores in 2D nanostructures through simple and controllable methods.

Owing to the high surface areas and large pore volumes, mesoporous materials have exhibited significant potentials in many applications, including catalysis, separation, energy conversion and storage.[30-37] Although recently well-established self-assembly techniques provide possibilities for producing diverse architectures, most of mesoporous materials reported are three-dimensional (3D) assembled mesostructures. The construction of mesostructures in combination with 2D morphologies remains a great challenge because this requires not only delicate control of assembly process, including hydrolysis of precursors, interaction between templates and sources, but also better understanding over the sophisticated molecular building blocks. Toward this end, the feasible method to achieve 2D mesoporous nanomaterials so far is to introduce solid 2D interfaces into reaction systems. By using flat substrates,[38, 39] or free-standing surfaces[40, 41] as hard templates and block copolymers as soft templates, the micelles are able to be assembled into 2D mesoporous materials at the solid-liquid phase interface. However, the directionality of 2D assembly can only be occurred at the limited interfaces between the hard templates and precursor solution, which bring about huge limitations such as low production as well as the difficulty of exfoliation from hard templates. Therefore, the exploration of facile chemical methods for controllable synthesis of 2D mesoporous materials in a scalable manner, which can in essence change conventional 3D assembly nature, remains highly desired.

In this paper, we demonstrate a facile hydrothermal-induced solvent-confined assembly approach for the first time to synthesize single-layered 2D ordered mesoporous TiO_2 nanosheets. To be specific, the acidic precursor solution containing solvent tetrahydrofuran (THF), titanium source tetrabutyl titanate (TBOT) and amphiphilic triblock copolymer Pluronic F127 was prepared initially. After evaporation of THF at a low temperature of 45 °C, the precursor solution turned into a viscous gel. The gel was subsequently dispersed in mixed solvents of ethanol and glycerol, followed by a hydrothermal treatment at 100 °C. Notably, the assembly process of monomicelles is entirely occurred under the guidance of surrounding glycerol in spatially confined 2D direction without usage of any solid interfaces. The obtained mesoporous TiO_2

nanosheets after the removal of the amphiphilic block copolymer template have a size with about 500 nm in both length and width, ~5.5 nm in thickness and comprised of only one layer of mesopores. The unique 2D mesoporous TiO_2 nanosheets can be used for sodium-ion battery, showing an excellent reversible capacity of 220 mAh g^{-1} at 0.1 A g^{-1}. At varied current densities from 0.1 to 10 A g^{-1}, the reversible capacities are still highly stable. Even at a high current density of 10 A g^{-1}, a stabilized capacity of 44 mAh g^{-1} and a high coulombic efficiency of ~97% are retained after 10000 cycles.

EXPERIMENTAL SECTION

Synthesis of Spherical F127/TiO_2 Composite Monomicelles. In a typical procedure, 1.5 g of Pluronic F127 ($PEO_{106}PPO_{70}PEO_{106}$, Mw = 12600 g mol^{-1}, Acros Corp.), 2.4 g of acetic acid and 3.5 g of concentrated HCl (36 wt%) were added in 30 mL of tetrahydrofuran (THF). After vigorously stirring for 10 min, 3.4 g of tetrabutyl titanate (TBOT, Sigma-Aldrich Corp.) was added dropwise and 0.20 g of H_2O was added subsequently. The formed clear white yellow solution was transferred into two 30 mm × 50 mm volumetric flasks, and left in a drying oven at 45 °C for 24 h.

Synthesis of Single-Layered 2D Mesoporous TiO_2 Nanosheets. In a typical procedure, 1.0 g of above obtained light yellow gel was added into 15 mL of ethanol with vigorous stirring to form a transparent solution. Then 15 mL of glycerol was added dropwise under vigorous stirring. After 10 min, the obtained transparent solution was transferred into a 50-ml autoclave. After heating at 100 °C for 10 h, the solution was allowed to cool down to room temperature naturally. The white precipitates was collected after centrifugation, washed with ethanol, and then dried in oven. Finally, the single-layered 2D mesoporous TiO_2 nanosheets were obtained by further calcination at 350 °C for 6 h in N_2. The products can be separated by simple 5 minutes' ultrasonic treatment.

The syntheses were repeated with the same conditions as that of single-layered 2D mesoporous TiO_2 nanosheets except for changing the solvent ratio of ethanol and glycerol. Typically, 1.0 g of prepared

monomicelle gel was added into 15, 20, 25 and 28 mL of ethanol, respectively. After stirring, 15, 10, 5 and 2 mL of glycerol were added dropwise. The total volumes of mixed solutions are kept at 31 mL. In addition, the syntheses were also conducted with changing the monomicelle concentration. Typically, 1.0, 2.0 and 3.0 g of prepared monomicelle gel were added into 15 mL of ethanol, respectively. After stirring, 15 mL of glycerol was added dropwise. The total volumes of mixed solutions are estimated to be 31, 32 and 33 mL. All of the synthetic parameters are listed in Supplementary Table 1.

Characterization and Measurements. Transmission electron microscopy (TEM) measurements were conducted on a JEM-2100 F microscope (JEOL, Japan) operated at 200 kV. Field-emission scanning electron microscopy (FESEM) images were taken on a Hitachi Model S-4800 microscope. Samples used for TEM and FESEM analyses were prepared by dropping of the TiO_2 dispersion in ethanol on amorphous carbon-coated copper grids and silicon substrates, respectively. Atomic force microscopy (AFM) measurements were performed in tapping mode (Multimode IV, Veeco) after depositing the samples on a mica. A silicon cantilever (TESP-SS, Veeco) with a normal tip radius of <5 nm was used after cleaning in UV/ozone for 15 min. Synchrotron radiation small-angle X-ray scattering (SAXS) measurements were performed at Beamline BL16B of Shanghai Synchrotron Radiation Facility (SSRF). The *d*-spacing values were calculated from the formula $d = 2\pi/q$. SAXS measurements were taken on a Nanostar U small-angle X-ray scattering system (Bruker, Germany) using $Cu_{K\alpha}$ radiation (40 kV, 35 mA). Wide-angle X-ray diffraction (WAXRD) patterns were recorded with a Bruker D8 powder X-ray diffractometer (Germany) using Cu Kα radiation (40 kV, 40 mA). Thermogravimetry analysis was conducted on a Mettler Toledo TGA/SDTA851 analyzer from 30 to 800 °C in air (20 mL/min) with a ramp rate of 5 °C/min. Nitrogen sorption isotherms were measured at 77 K with a Micromeritics Tristar 3020 analyzer (USA). Before measurements, the samples were degassed in a vacuum at 180 °C for at least 12 h. The Brunauer-Emmett-Teller (BET) method was utilized to calculate the specific surface areas. The pore volumes and pore size distributions were derived from the adsorption branches of isotherms using the

Barrett-Joyner-Halenda (BJH) model. (XPS) was recorded on an AXIS ULTRA DLD XPS System with MONO Al source (Shimadzu Corp). Photoelectron spectrometer is recorded by using monochromatic Al K_R radiation under vacuum at 5×10^{-9} Pa. All callibrations were referenced to the surface adventitious carbon (C_{1s} = 284.6 eV).

Electrochemical Measurements. Electrochemical properties were tested by using a CR2016 coin cell. The anode electrode materials were prepared by mixing 80 wt% of the 2D mesoporous TiO_2 nanosheets, 10 wt% of carbon black as a conductive agent and 10 wt% of sodium carboxymethylcellulose (CMC-Na, Sigma-Aldrich Corp.) as a binder. The electrode films were obtained by casting the slurry on a Cu foil. Then, the electrodes were dried at 80 °C for 12 h in a vacuum oven. Sodium metal was the counter and reference electrode. 1.0 M of $NaClO_4$ (AR, Sigma-Aldrich Corp.) was dissolved in ethylene carbonate (EC) and propylene carbonate (PC) in a volume ratio of 1:1 was used as the electrolyte. Whatman glass microfibre filter (Grade GF/C) was used as a separator (which was supplied by the Whatman Corp.; EC and PC were purchased from Shanghai Xiaoyuan Energy Corp. Ltd). The typical mass loading of the active material was about 2 mg cm^{-2}. All coin cells were assembled in an argon-filled glove box. Electrochemical tests including rate performance and cycling performance were performed on the HOKUTO DENKO Battery Charge/Discharge System HJ Series controlled by a computer. The voltage window was 0.01-3.0 V. Cyclic voltammetry (CV) tests were carried out by using the three-electrode customized-cell. The CV measurements were performed on a Princeton chemical work station (PARSTAT MC-500, USA.). All electrochemical measurements were tested at room temperature (25 °C).

RESULTS AND DISCUSSION

Structure of single-layered 2D mesoporous TiO_2 nanosheets. The ordered 2D mesoporous TiO_2 nanosheets with a uniform thickness of single layer of mesopores can be assembled through the hydrothermal-induced solvent-confined monomicelle assembly process. As shown in field emission

scanning electron microscopy (FESEM) image (Figure 1a), the mesoporous TiO_2 nanosheets in well-retained 2D morphology are random stacked into a bulk. No unassembled irregular TiO_2 nanoparticles can be observed perhaps due to the fast hydrolysis, indicating the superiority of such hydrothermal-induced solvent-confined assembly method. The uniform mesoporous TiO_2 nanosheets are composed of slightly curved slices with ~500 nm in length and ~500 nm in width (Figure 1b). The uniform mesopores in the TiO_2 nanosheets can be observed and the thickness of these nanosheets is within a few nanometers (Figure 1c, d).

The mesoporous TiO_2 nanosheets were separated by simple ultrasonic treatment for further characterizations. The transmission electron microscopy (TEM) image shows that the size of the mesoporous TiO_2 nanosheets is in the range of 200 to 500 nm (Figure 2a). Most of the nanosheets consist of single-layered mesopores, although a few of them are dual-layered (red circles in Figure 2a). The stacked nanosheets can be observed and the thickness is measured to be around 8.5 nm, indicating the dual-layered structure (Figure S1a, b). These nanosheets clearly possess well-defined ordered mesostructures with a mean pore size of around 4 nm (Figure 2b-d, Figure S2), which is ascribed to the framework shrinkage during calcination at 350 °C in N_2. The atomic force microscopy (AFM) tomography (Figure 2e) and phase images (Figure S1c) in tapping mode reveal that the mesoporous TiO_2 nanosheets have rough surfaces with an approximate thickness of 5.5 nm. The mesopore size of ~4 nm is slightly smaller than the thickness, implying that only one layer of mesopores is close-packed in 2D plane (Figure S1d). The high-resolution TEM (HRTEM) image shows that the pore walls of the mesoporous TiO_2 nanosheets are comprised of well crystallized TiO_2 nanoparticles with a *d*-spacing of 0.35 nm, corresponding to the (101) plane of anatase (Figure 2f). The selected area electronic diffraction (SAED) pattern displays well-resolved diffraction rings and numerous spots (Inset of Figure 2f), further indicating a crystallized anatase nanosheets. From the integrated energy dispersive X-ray spectroscopy (EDS) analysis elemental mapping performed on a single mesoporous TiO_2 nanosheet (Figure S3a-d), Ti, O and C elements are very uniformly distributed. The thermogravimetry (TG) curve of the mesoporous TiO_2 nanosheets shows a weight loss of 2.3% at around

150 °C, assigned to adsorbed water, and a weight loss of 15.5% at 800 °C (Figure S3e), indicating that the weight of residual carbon rooted in carbonized surfactant is about 13.2%. Additionally, the mesoporous TiO_2 nanosheets after being calcined in air at 400 °C for 3 h are composed of relative large TiO_2 nanoparticles of around 10 nm and possess no mesopores although they can keep 2D morphology (Figure S4), suggesting that the residual carbon is necessary to prevent the collapse of the mesopore frameworks.

The wide-angle X-ray diffraction (WAXRD) pattern (Figure S3a) shows well-defined diffraction peaks at 25.5, 37.8, 48.0, 53.8, 55.2, and 62.9°, which can be indexed to the 101, 004, 200, 105, 211 and 204 reflections of anatase, demonstrating the highly crystalline anatase phase (space group $I4_1/amd$) of the 2D mesoporous TiO_2 nanosheets. The TiO_2 grain size is calculated from Scherrer equation to be 2.3 nm, consistent with that (2.4 nm) observed from HRTEM results (Figure S5). The small-angle X-ray scattering (SAXS) pattern of the 2D mesoporous TiO_2 nanosheets shows broad and weak scattering peaks, mainly due to the ultrathin thickness and random stacking between individual nanosheets (Figure S6). The scattering peaks at q-value of around 0.070, 0.114, 0.136 nm^{-1} should be indexed to the 100, 200 and 210 reflections of hexagonal mesostructure with the space group *p6mm*. Nitrogen adsorption-desorption isotherms reveal characteristic type IV curves with distinguishable capillary condensation step at P/P_0 = 0.5 to 1.0 (Fig. 3b), suggesting that the TiO_2 nanosheets contain uniform mesopores. The Brunauer-Emmett-Teller (BET) surface area and pore volume of the 2D mesoporous TiO_2 nanosheets are calculated to be as high as 210 m^2 g^{-1} and 0.35 cm^3 g^{-1}, respectively. The corresponding pore size distribution curves (Figure 3c) derived from the adsorption branches of the isotherms by using the Barrett-Joyner-Halenda (BJH) method clearly show a centered pore size at 4.0 nm, in agreement with the TEM results. X-ray photoelectron spectroscopy (XPS) of O1s shows two chemical states. The sharp peak at 530.7 eV and broad peak at 532.7 eV can be assigned to O-Ti bonds and O-H bonds, respectively (Figure 3d), suggesting massive Ti-OH groups on the surface of the 2D mesoporous TiO_2 nanosheets.[42] The Ti2p XPS spectrum (Figure 3e) shows two peaks at 465.5 eV (Ti2p1/2) and 459.5 eV (Ti2p3/2), assigned to Ti^{4+} oxidation states.[43] For C1s XPS spectrum (Figure 3f), the

major peak at 286.1 eV is attributed to the surface C-C bonds, the second peak at 290.3 eV is from carbon atoms presented in surface C-OH or C-O-C groups, and the third peak at 293.8 eV is contributed from -COOH or -COO- groups.[44, 45]

It is found that the thickness of the mesoporous TiO_2 nanosheets can well be tuned by simply varying ethanol/glycerol solvent ratio or precursor concentration (Table S1). With the increase of ethanol/glycerol ratio, the thickness of the TiO_2 nanosheets increases rapidly and the surface area decreases dramatically. The TiO_2 nanosheets possess a thickness of single-layered mesopores when the solvent ratio is 1:1. When the ethanol/glycerol ratio increases to 2:1, the well-defined 2D morphology of the mesoporous TiO_2 nanosheets can be observed (Figure S7a). After ultrasonic treatment, the TEM images and SAED pattern clearly reveal a large porosity and good crystallinity (Figure S7b-d). The BET surface area is calculated to be 178 $m^2 g^{-1}$. An estimated thickness of around 11.5 nm from the side-view TEM image of a nanosheet (Figure S7e) is in good accord with the thickness of 12.4 nm measured by AFM (Figure S7f), corresponding to three layers of mesopores. When the solvent ratio increases to 5:1, the mesoporous TiO_2 nanosheets with a thickness of around 25.5 nm can be obtained (Figure S8a, b), and their BET surface area is 154 $m^2 g^{-1}$. Furthermore, when solvent ratio turns to 14:1, the surface area is further decreased to 131 $m^2 g^{-1}$. SEM images show that a mixture of microspheres and stacked nanosheets are formed (Figure S9a, b). These results suggest that glycerol plays a decisive role for the formation of uniform 2D mesoporous TiO_2 nanosheets. On the other hand, with the increase of the precursor concentration, the thickness of the mesoporous TiO_2 nanosheets can increase either, from 5.5 to 27.6 nm (Table S1). Moreover, the mesopore size of 2D ordered mesoporous TiO_2 nanosheets can be enlarged to some extent by adding trimethylbenzene (TMB) as a swelling agent. The mesopore size of the obtained mesoporous TiO_2 nanosheets is increased from 7.4 to 12.5 nm when TMB amount increased from 0.5 to 2.0 mL, which is proven by the corresponding pore size distribution curves. (Figure S10).

Formation mechanism studies. When repeating the syntheses using the same recipes at room temperature

and 80 °C, the solutions remains transparent and no precipitates can be obtained (Figure S11a, b). The spherical monomicelles still dominate with no lamellar morphology, confirming that a sufficient thermodynamic driving force is required for triggering the assembly process (Figure S11c, d). The syntheses were also conducted using other solvents instead of glycerol. With the addition of pure ethanol as a solvent, non-uniform mesoporous TiO_2 microspheres are formed (Figure S12a). Furthermore, when glycerol is replaced by other solvents with hydroxyl groups, such as methanol, benzyl alcohol, glycol, isopropanol, no TiO_2 nanosheets but microspheres with irregular sizes can be obtained under the same hydrothermal condition (Figure S12b-e). Moreover, TiO_2 microspheres and TiO_2 bulks can be observed after the hydrothermal treatment when using glucose-saturated water or polyethylene glycol (PEG) with varied molecular weight to substitute glycerol (Figure S12f-h). Hence, glycerol should perform as a special structure-directing-agent due to its intrinsic properties.

The assembly process was studied by terminating reaction at different intervals. *Ex-situ* TEM images (Figure S13a-d) show that spherical PEO-PPO-PEO monomicelles with a uniform diameter of around 6.5 nm surrounded by the TiO_2 oligomers are formed after THF evaporation at 45 °C for 24 h. *In-situ* synchrotron radiation SAXS patterns were utilized to examine the samples harvested at varied intervals of reaction. As shown in the 2D SAXS pattern (Figure S14a), a broad scattering peak at $q = 0.4$ nm^{-1} is detected after THF evaporation at 45 °C for 12 h. The intensity of peaks increase rapidly with the evaporation time prolongs from 0 to 24 h, which is attributed to increased electron density contrast due to the adsorption of TiO_2 oligomers to PEO groups (Figure S14b). The shift to higher q value of reflections with solvent evaporation from 0 to 24 h corresponds to a decline of unit cell parameter owing to an increase of TiO_2 condensation. The diameter of spherical PEO-PPO-PEO monomicelles decreases from 10.5 to 6.5 nm when TiO_2 oligomers further condense from 12 to 24 h (Figure S15), consistent with the 1D SAXS results. It is speculated that when the hydrolysis reaction proceeds for longer time, the TiO_2 oligomers might have a more dense structure, leading to a higher degree of condensation.[46] Besides, the structure of the composite

monomicelles are well-retained after dispersed in the mixed solution of ethanol and glycerol although their packing is not very ordered, implying that the monomicelles are surrounded by glycerol due to the strong hydrogen bonding (Figure S16). After the hydrothermal reaction of such monomicelles in ethanol/glycerol solution over 3 h, the morphology of the products displays web-like structure comprised of linear monomicelles (Figure S17). When the reaction is terminated at 6 h, the stacked TiO_2 nanosheets with curved planes are formed (Figure S18a, b). Notably, there are no impurities (unassembled and irregular small TiO_2 nanoparticles) observed, clearly indicating that all of the spherical monomicelles in solution are assembled into TiO_2 nanosheets. Such ultrahigh purity is because not only the closed space can deny the contact with extra water in air, but also the surrounding glycerol has much strong interaction, thus enabling to eradicate the appearance of small particles due to fast hydrolysis.

On the basis of the above observations, the formation mechanism of the single-layered 2D ordered mesoporous TiO_2 nanosheets can be proposed as a hydrothermal-induced solvent-confined monomicelle assembly process (Figure 4). With the evaporation of THF at a low temperature, the precursor TBOT is hydrolyzed slowly and assembled with amphiphilic Pluronic triblock copolymer F127 into very uniform spherical monomicelles as subunits, as confirmed by *Ex-situ* TEM images. When dispersed in a mixed solution of ethanol and glycerol, the Pluronic F127/TiO_2 composite spherical monomicelles are tightly surrounded by glycerol due to the strong hydrogen bonding between the –OH groups of titania oligomers and three hydroxyl groups of glycerol molecules. During the hydrothermal treatment, the glycerol between assembled monomicelles moves away owing to the mechanically unstable state[47] and the titania oligomers continue to hydrolyze and condense together. When the dimer or/and trimer chains of spherical monomicelles can be confined with glycerol-rich domains and assemble as units, their translational motions along the tangential direction dominate and the angular velocities decrease drastically because the adhered glycerol can severely decrease the thermal mobility in the normal direction due to its high interfacial viscosity (Step 1).[48, 49] After continuous collision, these F127/TiO_2 spherical composite monomicelles

collide head-to-head into the linear arrays which further elongate and crosslink into a large web-like framework (Step 2). With the hydrothermal reaction proceeds, the dissociative monomicelles start to assemble randomly at the side of linear framework and tend to pack close one by one driven by the stronger hydrogen interaction of adjacent monomicelles. Owing to the surrounded high-viscosity glycerol, the velocity of the tetramer and pentamer monomicelle units at the side of the linear chains is concentrated on the low-density parallel direction.[47] The collisions can only be occurred in glycerol-confined parallel direction, leading to enlarged 2D domains at different nodes (Step 3). It is worthwhile to note that the 2D domains are compelled to pack nearly in a parallel direction in order to reduce flow resistance of the thermal motion along tangential direction, thereby forming a slight curved 2D plane when these domains further assemble (Step 4). Subsequently, a single layer of the monomicelles is formed within the confined 3D high-viscosity glycerol networks after further assemble in parallel direction. The single-layered mesoporous nanosheets are finally obtained after crystallization and removal of template by high-temperature calcination in an inert environment. Moreover, the decreased amount of glycerol (lower monomicelle concentration or higher ethanol/glycerol solvent ratio) can lead to the weakened confinement effect, thus the assembling tendency in perpendicular direction is gradually favored, resulting in the multilayer growth of the monomicelles and even 3D mesostructures (Figure S19).

Electrochemical properties of single-layered 2D mesoporous TiO_2 nanosheets. Due to the unique structural features, the electrochemical performances of the 2D mesoporous TiO_2 nanosheets as a sodium-ion battery were investigated. During the initial negative scan, the cathodic peak is located at about 0.8 V (Figure S20), which is mainly ascribed to the formation of solid electrolyte interface (SEI) film due to the decomposition of reductive electrolytes.[50, 51] In the first anodic scan, the broad peak in the range of 0.5-1.2 V is observed, which is assigned to the Ti^{3+}/Ti^{4+} redox couple. In the following 2^{nd}, 5^{th} and 10^{th} sweep process, peak current density and integrated area intensity are nearly unchanged, indicating that the 2D mesoporous TiO_2 nanosheets show tiny capacity losses during cycling. In addition, the current flowing at

a low potential of 0.4 V can be associated with the partial conversion of TiO_2 into metallic titanium and sodium peroxide as well as the formation of sodium titanate.[52]

From the charge-discharge curves of the electrode cycled at 0.1 A g^{-1} (Figure 5a), a pair of broad slopes at 0.1-0.8 V (for the discharge process) and at 0.5-1.0 V (for the charge process) in all cycles are observed, corresponding to the reversible sodiation and desodiation reactions,[52] which is in good accord with the CV results. The initial discharge and charge capacity is as high as 317 and 190 mAh g^{-1}, respectively. The resultant initial coulombic efficiency of the 2D mesoporous TiO_2 nanosheets is up to 60%, much higher than that of commercial rutile TiO_2 anodes and carbon modified anatase TiO_2 anodes.[53] It is observed that the charge capacity presents a gradually increased range from 190 to 202 mAh g^{-1} over 1-50 cycles, which is mainly attributed to the activation process and suppressed side reactions.[54, 55] The capacity after 100 cycles can still reach 197 mAh g^{-1}, demonstrating the great cyclability at a low rate. The Coulombic efficiency goes up rapidly to 97% in the 10 cycle and retains at this level for the following cycles.

Meanwhile, the 2D mesoporous TiO_2 nanosheets show outstanding rate and cycling performance. At a current density of 100 mA g^{-1}, the reversible capacity is calculated to be around 220 mAh g^{-1} (Figure 5b, c). The reversible capacities can be stabilized at 183, 156, 136, 119 and 88 mAh g^{-1} at current density of 0.2, 0.5, 1.0, 2.0 and 5 A g^{-1}, respectively. At an ultrahigh current density of 10 A g^{-1}, a stable reversible capacity of 67 mAh g^{-1} is observed, suggesting the excellent rate capability. Notably, after 70 cycles at varied current densities, the capacity is retained at 199 mAh g^{-1} when the current density is reset to 0.1 A g^{-1}. In order to test the cycling performance of the uniform 2D mesoporous TiO_2 nanosheets at high rates, a sodium cell using such material was evaluated under current density of 10 A g^{-1} (Figure 5d). The initial discharge capacity starts at 63 mAh g^{-1} and remains at 44 mAh g^{-1} after 10000 cycles, corresponding to a retention ratio of 70%. In addition, the coulombic efficiency is near to 97% for each cycle, showing the great structure stability in ultra-long cycles even at a high current density.

The uniform single-layered 2D mesoporous TiO_2 nanosheets exhibit excellent sodium ion storage

capacity, outstanding rate performance and great cycling stability, which are mainly attributed to the unique 2D mesostructure with ultrathin thickness and high accessible surface area. The abundant mesopores of the 2D TiO_2 nanosheets and high accessible specific surface area make the TiO_2 nanosheets highly permeable for comprehensive electrode-electrolyte contact externally and internally, thereby leading to rapid electrochemical reactions and providing high reversible sodium ion storage capacities. The thin mesopore walls with well-crystalline anatase structure enable to shorten the diffusion lengths of sodium ions. More importantly, the sodium ions are compelled to transport in confined 2D space during intercalation-extraction process due to the reduction of dimensions and the ultrathin single-layered structure, which promotes the charge transfer to a large extent. In addition, the mesoporous well-crystalline anatase frameworks can offer great accommodation to volume strain changes during sodium insertion-extraction. All these structural features contribute to the outstanding rate performance and superior cycling stability at a high current density.

CONCLUSIONS

In summary, we have demonstrated a hydrothermal-induced solvent-confined monomicelles assembly approach to synthesize novel single-layered mesoporous TiO_2 nanosheets. The initially formed F127/TiO_2 monomicelles are dispersed in ethanol/glycerol mixed solution and assemble into single-layered 2D mesostructure under a simple hydrothermal treatment because of the parallel network domain confinement of the highly viscous glycerol solvent. These uniform nanosheets are around 500 nm in both length and width, ~5.5 nm in thickness and composed of only one layer of mesopores. The 2D mesoporous TiO_2 nanosheets possess a very high surface area (154-210 m^2 g^{-1}), large pore volume (0.29-0.35 cm^3 g^{-1}), uniform mesopore channels (3.8-4.1 nm) and well-crystalline anatase mesopore walls. The thickness of the 2D mesoporous TiO_2 nanosheets can well be manipulated from 5.5 to 27.6 nm by simply tuning the concentration or ethanol/glycerol ratio. The sodium-ion battery anode made of these uniform 2D

mesoporous TiO_2 nanosheets exhibit very excellent electrochemical performances, including large discharge specific capacity of 220 mAh g^{-1} at 100 mA g^{-1}, outstanding rate capability (stable reversible capacities from 0.1 to 10 A g^{-1}), as well as ultra-long cycling stability (44 mAh g^{-1} for 10000 cycles at 10 A g^{-1}). The spatially confined assembly based on viscous solvent in preferred 2D direction can be motivated *via* a simple thermodynamic driving force with no tedious procedures or harsh conditions, making this new approach highly flexible and applicable for further potential explorations. We envisage that such unprecedented confined 2D assembly technique affords us a new methodology to control the morphology and mesostructural regularity in solution, which can be extended to fabricate a family of novel 2D nanoporous materials such as ZrO_2, SnO_2, Al_2O_3, etc.

ASSOCIATED CONTENT

Supporting Information

The Supporting Information is available free of charge on the ACS Publications website.

Figures S1-S20, Table S1

AUTHOR INFORMATION

Corresponding Author

dyzhao@fudan.edu.cn

Notes

The authors declare no competing financial interests.

ACKNOLEDGMENTS

This work was supported by the State Key Basic Research Program of China (2017YFA0207303), the National Science Foundation of China (21733003), Science and Technology Commission of Shanghai Municipality (17JC1400100), and Shanghai Leading Academic Discipline Project (B108). The authors

extend their appreciation to the International Scientific Partnership Program ISPP at King Saud University for funding this research work through ISPP# 0018.

REFERENCES

(1) Novoselov, K. S.; Geim, A. K.; Morozov, S. V.; Jiang, D.; Zhang, Y.; Dubonos, S. V.; Grigorieva, I. V.; Firsov, A. A. *Science* **2004,** 306, 666.

(2) Meyer, J. C.; Geim, A. K.; Katsnelson, M. I.; Novoselov, K. S.; Booth, T. J.; Roth, S. *Nature* **2007,** 446, 60.

(3) Chhowalla, M.; Shin, H. S.; Eda, G.; Li, L. J.; Loh, K. P.; Zhang, H. *Nat. Chem.* **2013,** 5, 263.

(4) Huang, X.; Zeng, Z. Y.; Zhang, H. *Chem. Soc. Rev.* **2013,** 42, 1934.

(5) Tan, C. L.; Cao, X. H.; Wu, X. J.; He, Q. Y.; Yang, J.; Zhang, X.; Chen, J. Z.; Zhao, W.; Han, S. K.; Nam, G. H.; Sindoro, M.; Zhang, H. *Chem. Rev.* **2017,** 117, 6225-6331.

(6) Zhang, H. *ACS Nano.* **2015,** 9, 9451-9469.

(7) Deng, D. H.; Novoselov, K. S.; Fu, Q.; Zheng, N. F.; Tian, Z. Q.; Bao, X. H. *Nat. Nano.* **2016,** 11, 218.

(8) Gao, S.; Lin, Y.; Jiao, X. C.; Sun, Y. F.; Luo, Q. Q.; Zhang, W. H.; Li, D. Q.; Yang. J. L.; Xie, Y. *Nature* **2016,** 529, 68.

(9) Liu, P. X.; Zhao, Y.; Qin, R. X.; Mo, S. G.; Chen, G. X.; Gu, L.; Chevrier, D. M.; Zhang, P.; Guo, Q.; Zang, D. D.; Wu, B. H.; Fu, G.; Zheng, N. F. *Science* **2016,** 352, 797.

(10) Feng, B. J.; Zhang, J.; Zhong, Q.; Li, W. B.; Li, S.; Li, H.; Cheng, P.; Meng, S.; Chen, L.; Wu, K. H. *Nat. Chem.* **2016,** 8, 563.

(11) Cullen, P. L.; Cox, K. M.; Subhan, M. K. B.; Picco, L.; Payton, O. D.; Buckley, D. J.; Miller, T. S.; Hodge, S. A.; Skipper, N. T.; Tileli, V.; Howard, C. A. *Nat. Chem.* **2017,** 9, 244.

(12) Fan, X. B.; Xu, P. T.; Li, Y. G. C.; Zhou, D. K.; Sun, Y. F.; Nguyen, M. A. T.; Terrones, M.; Mallouk, T. E. *J. Am. Chem. Soc.* **2016,** 138, 5143.

(13) Yang, S. B.; Feng, X. L.; Mullen, K. *Adv. Mater.* **2011,** 23, 3575.

(14) Zeng, Z. Y.; Yin, Z. Y.; Huang, X.; Li, H.; He, Q. Y.; Lu, G.; Boey, F.; Zhang, H. *Angew. Chem. Int. Ed.* **2011,** 50, 11093.

(15) Wang, S.; Wang, Q. Y.; Shao, P. P.; Han, Y. Z.; Gao, X.; Ma, L.; Yuan, S.; Ma, X. J.; Zhou, J. W.; Feng, X.; Wang, B. *J. Am. Chem. Soc.* **2017,** 139, 4258.

(16) Tan, C. L.; Lai, Z. C.; Zhang, H. Adv. Mater. 2017, 29, 1701392.

(17) Chen, S.; Duan, J. J.; Vasileff, A.; Qiao, S. Z. *Angew. Chem. Int. Ed.* **2016,** 55, 3804.

(18) Zhu, D. D.; Guo, C. X.; Liu, J. L.; Wang, L.; Du, Y.; Qiao, S. Z. *Chem. Commun.* **2017,** 53, 10906.

(19) Jiang, L. L.; Fan, Z. J. *Nanoscale,* **2014,** 6, 1922.

(20) Colson, J. W.; Dichtel, W. R. *Nat. Chem.* **2013,** 5, 453.

(21) Perepichka, D. F.; Rosei, F. *Science* **2009,** 323, 216.

(22) Peng, Y. W.; Huang, Y.; Zhu, Y. H.; Chen, B.; Wang, L. Y.; Lai, Z. C.; Zhang, Z. C.; Zhao, M. T.; Tan, C. L.; Yang, N. L.; Shao, F. W.; Han, Y.; Zhang, H. *J. Am. Chem. Soc.* **2017,** 139, 8698-8704.

(23) Bieri, M.; Treier, M.; Cai, J. M.; Ait-Mansour, K.; Ruffieux, P.; Groning, O.; Groning, P.; Kastler, M.; Rieger, R.; Feng, X. L.; Mullen, K.; Fasel, R. *Chem. Commun.* **2009,** 6919.

(24) Liu, W.; Luo, X.; Bao, Y.; Liu, Y. P.; Ning, G. H.; Abdelwahab, I.; Li, L. J.; Nai, C. T.; Hu, Z. G.; Zhao, D.; Liu, B.; Quek, S. Y.; Loh, K. P. *Nat. Chem.* **2017,** 9, 563.

(25) Bai, J. W.; Zhong, X.; Jiang, S.; Huang, Y.; Duan, X. F. *Nat. Nanotechnol.* **2010,** 5, 190.

(26) Zhu, Y. W.; Murali, S.; Stoller, M. D.; Ganesh, K. J.; Cai, W. W.; Ferreira, P. J.; Pirkle, A.; Wallace, R. M.; Cychosz, K. A.; Thommes, M.; Su, G.; Stach, E. A.; Ruoff, R. S. *Science* **2011,** 332, 1537.

(27) Liang, X. G.; Jun, Y. S.; Wu, S. W.; Ismach, A.; Olynick, D. L.; Cabrini, S.; Bokor, J. *Nano Lett.* **2010,** 10, 2454.

(28) Kim, M.; Safron, M. S.; Han, E.; Arnold, M. S.; Gopalan, P. *Nano Lett.* **2010,** 10, 1125.

(29) Sinitskii, A.; Tour, J. M. *J. Am. Chem. Soc.* **2010,** 132,14730.

(30) Li, W.; Liu, J.; Zhao, D. Y. *Nat. Rev. Mater.* **2016,** 16023.

(31) Bach, U.; Lupo, D.; Comte, P.; Moser, J.; Weissörtel, F.; Salbeck, J.; Spreitzer, H.; Grätzel, M. *Nature* **1998,** 395, 583.

(32) Yang, P. D.; Zhao, D. Y.; Margolese, I.; Chmelka, B. F.; Stucky, G. D. *Nature* **1998,** 396, 152.

(33) Crossland, E. J.; Noel, N.; Sivaram, V.; Leijtens, T.; Alexander-Webber, J. A.; Snaith, H. J. *Nature* **2013,** 495, 215.

(34) Wu, C. W.; Ohsuna, T.; Kuwabara, M.; Kuroda, K. *J. Am. Chem. Soc.* **2006,** 128, 4544.

(35) Liu, B.; Liu, L. M.; Lang, X. F.; Wang, H. Y.; Lou, X. W. *Energy Environ. Sci.* **2014,** 7, 2592.

(36) Guan, B. Y.; Yu, L.; Li, J.; Lou, X. W. *Sci. Adv.* **2016,** 2, e1501554.

(37) Liu, Y.; Luo, Y. F.; Elzatahry, A. A.; Luo, W.; Che, R. C.; Fan, J. W.; Lan, K.; Al-Enizi, A. M.; Sun, Z. K.; Li, B.; Liu, Z. W.; Shen, D. K.; Ling, Y.; Wang, C.; Wang, J. X.; Gao, W. J.; Yao, C.; Yuan, K. P.; Peng, H. S.; Tang, Y.; Deng, Y. H.; Zheng, G. F.; Zhou, G.; Zhao, D. Y. *ACS Cent. Sci.* **2015,** 1, 400.

(38) Fang, Y.; Lv, Y. Y.; Che, R. C.; Wu, H. Y.; Zhang, X. H.; Gu, D.; Zheng, G. F.; Zhao, D. Y. *J. Am. Chem. Soc.* **2013,** 135, 1524.

(39) Fang, Y.; Lv, Y. Y.; Gong, F.; Elzatahry, A. A.; Zheng, G. F.; Zhao, D. Y. *Adv. Mater.* **2016,** 28, 9385.

(40) Liu, S. H.; Gordiichuk, P.; Wu, Z. S.; Liu, Z. Y.; Wei, W.; Wagner, M.; Noriega, N. M.; Wu, D. Q.; Mai, Y. Y.; Herrmann, A.; Mullen, K.; Feng, X. L. *Nat. Commun.* **2015,** 6, 8817.

(41) Liu, S. H.; Zhang, J.; Dong, R. H.; Gordiichuk, P.; Zhang, T.; Zhuang, X. D.; Mai, Y. Y.; Liu, F.; Herrmann, A.; Feng, X. L. *Angew. Chem. Int. Ed.* **2016,** 55, 1.

(42) Liu, Y.; Che, R. C.; Chen, G.; Fan, J. W.; Sun, Z. K.; Wu, Z. X.; Wang, M. H.; Li, B.; Wei, J.; Wei, Y.; Wang, G.; Guan, G. Z.; Elzatahry, A. A.; Bagabas, A. A.; M. Al-Enizi, A. M.; Deng, Y. H.; Peng, H. S.; Zhao, D. Y. *Sci. Adv.* **2015,** 1, e1500166.

(43) Yang, H. G.; Liu, G.; Qiao, S. Z.; Sun, C. H.; Jin, Y. G.; Smith, S. C.; Zou, J.; Cheng, H. M.; Lu, G. Q. *J. Am. Chem. Soc.* **2009,** 131, 4078.

(44) Dou, J.; Zeng, H. C. *J. Phys. Chem. C* **2012,** 116, 7767.

(45) Biniak, S.; Szymanski, G.; Siedlewski, J.; Swiatkowski, A. *Carbon* **1997,** 35, 1799.

(46) Huo, Q. S.; Liu, J.; Wang, L. Q.; Jiang, B. B.; Lambert, T. N.; Fang, E. *J. Am. Chem. Soc.* **2006,** 128, 6447.

(47) Furukawa, A.; Tanaka, H. *Nature* **2006,** 443, 434.

(48) Pronk, S.; Lindahl, E.; Kasson, P. M. *Nat. Commun.* **2014,** 5, 4034.

(49) Vutukuri, H. R.; Bet, B.; Roij, R. V.; Dijkstra, M.; Huck, W. T. S. *Sci. Rep.* **2017,** 7, 16758.

(50) Tahir, M. N.; Oschmann, B.; Buchholz, D.; Dou, X. W.; Lieberwirth, I.; Panthöfer, M.; Tremel, W.; Zentel, R.; Passerini, S. *Adv. Energy Mater.* **2016,** 6, 1501489.

(51) Ye, C.; Zhang, L.; Guo, C. X.; Li, D. D.; Vasileff, A.; Wang, H. H.; Qiao, S. Z. *Adv. Funct. Mater.* **2017,** 27, 1702524.

(52) Wu, L. M.; Bresser, D.; Buchholz, D.; Giffin, G. A.; Castro, C. R.; Ochel, A.; Passerini, S. *Adv. Energy Mater.* **2015,** 5, 1401142.

(53) Zhang, Y.; Foster, C. W.; Banks, C. E.; Shao, L. D.; Hou, H. S.; Zou, G. Q.; Chen, J.; Huang, Z. D.; Ji, X. B. *Adv. Mater.* **2016,** 28, 9391.

(54) Xie, F. X.; Zhang, L.; Su, D. W.; Jaroniec, M.; Qiao, S. Z. *Adv. Mater.* **2017,** 29, 1700989.

(55) Su, D. W.; McDonagh, A.; Qiao, S. Z.; Wang, G. X. *Adv. Mater.* **2017,** 29, 1604007.

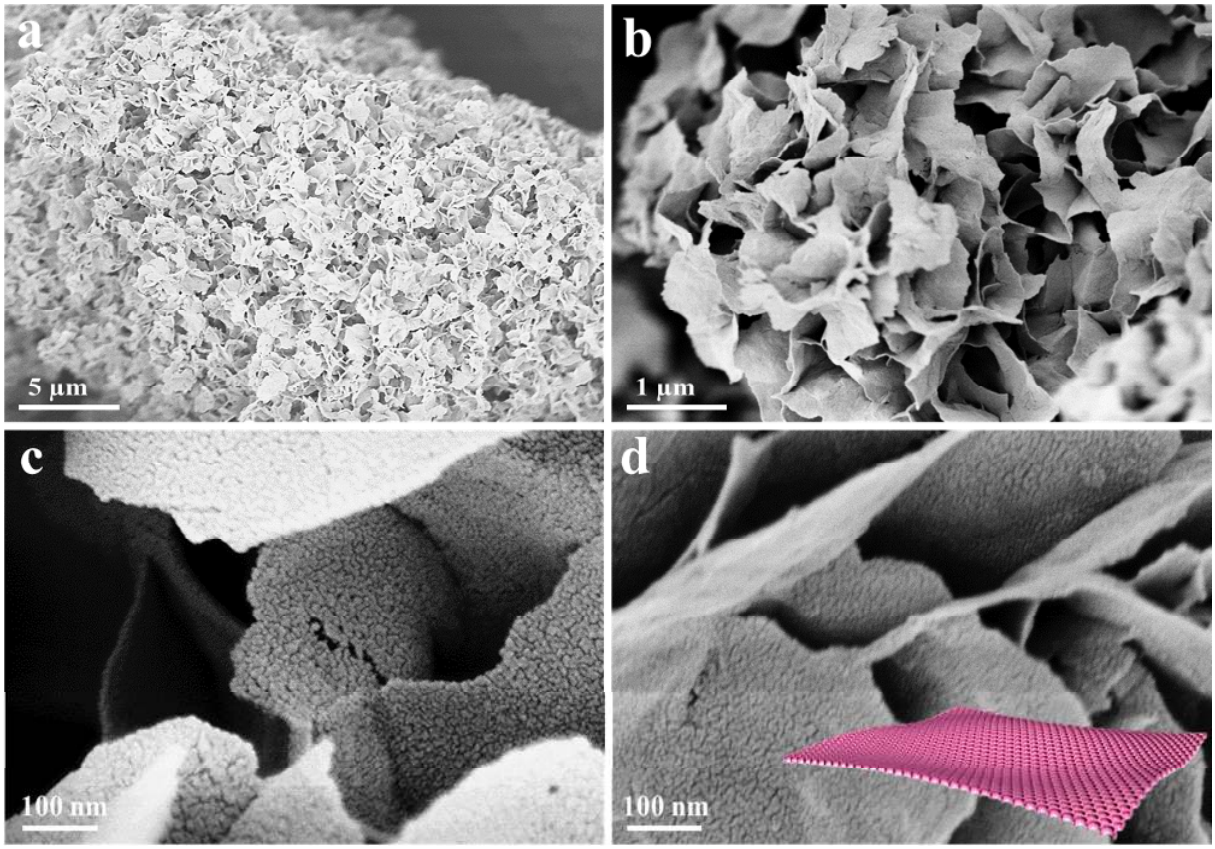

Figure 1. (a-d) SEM images with different magnifications of the single-layered 2D mesoporous TiO_2 nanosheets prepared by hydrothermal-induced solvent-confined monomicelle assembly approach at 100 °C for 10 h after the calcination in N_2 at 350 °C for 6 h. Inset of **(d)** is the corresponding structure model of the single-layered 2D mesoporous TiO_2 nanosheets.

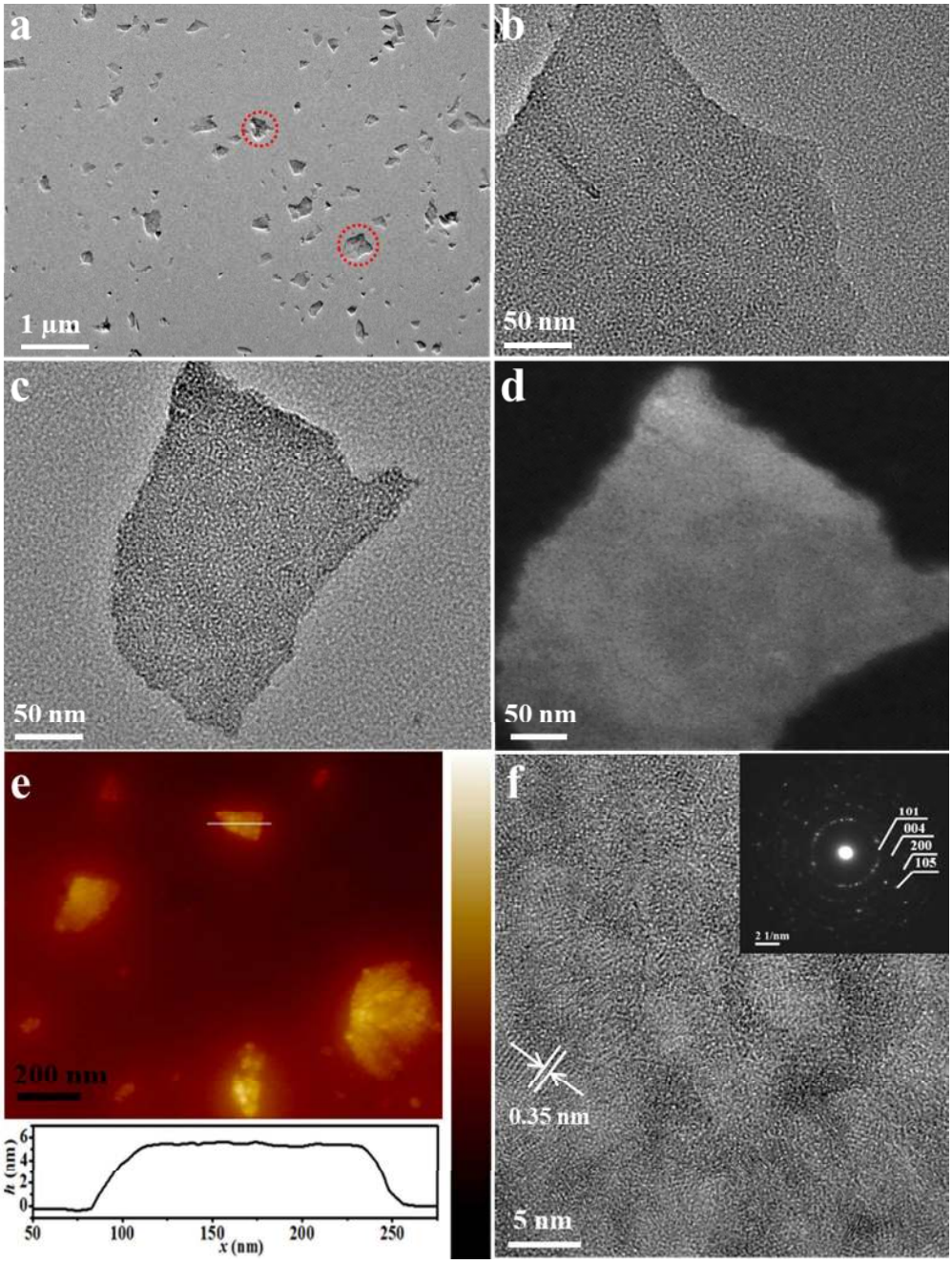

Figure 2. (a-c) TEM images with different magnifications and **(d)** HAADF image of the single-layered mesoporous TiO_2 nanosheets prepared by hydrothermal-induced solvent-confined monomicelle assembly approach at 100 °C for 10 h after the calcination in N_2 at 350 °C for 6 h. **(e)** AFM topography image and corresponding height information of the single-layered mesoporous TiO_2 nanosheets. The vertical scale is 11.8 nm. **(f)** HRTEM image of the single-layered mesoporous TiO_2 nanosheets. Inset of (f) is the SAED pattern taken from the nanosheet in panel (c).

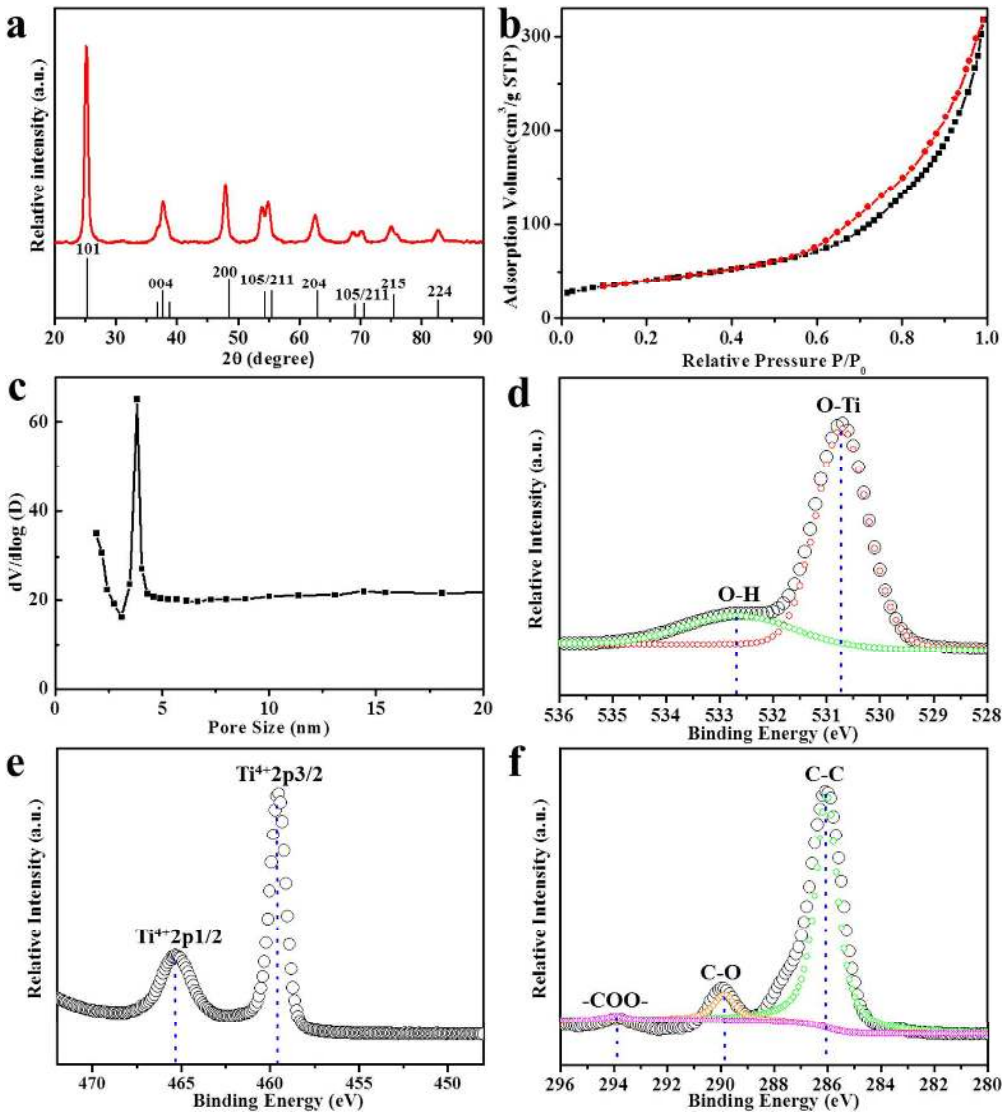

Figure 3. Characterization of the single-layered 2D ordered mesoporous TiO_2 nanosheets prepared by hydrothermal-induced solvent-confined monomicelle assembly approach at 100 °C for 10 h after the calcination in N_2 at 350 °C for 6 h. **(a)** WAXRD pattern of the 2D mesoporous TiO_2 nanosheets, compared to the standard anatase (space group $I4_1/amd$, JCPDS card No. 21-1272. **(b)** Nitrogen adsorption-desorption isotherms and **(c)** Pore size distribution of the mesoporous TiO_2 nanosheets. **(d-f)** XPS core-level spectra of O1s, Ti2p and C1s for the mesoporous TiO_2 nanosheets, respectively.

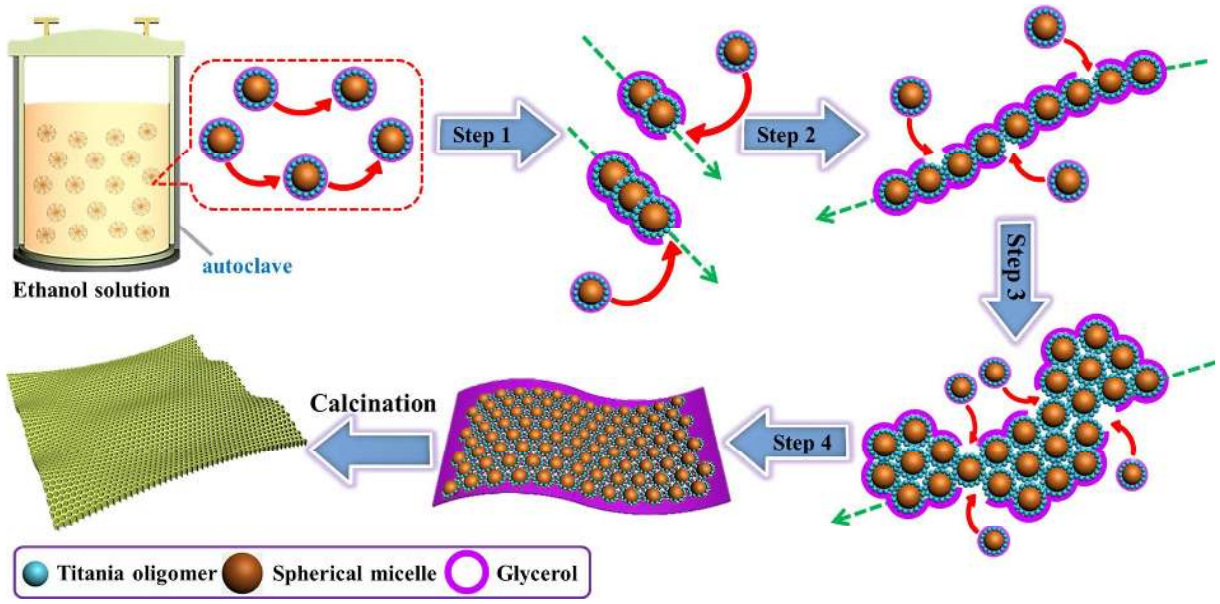

Figure 4. Schematic illustration of the formation process for the single-layered 2D ordered mesoporous TiO_2 nanosheets *via* hydrothermal-induced solvent-confined monomicelle assembly.

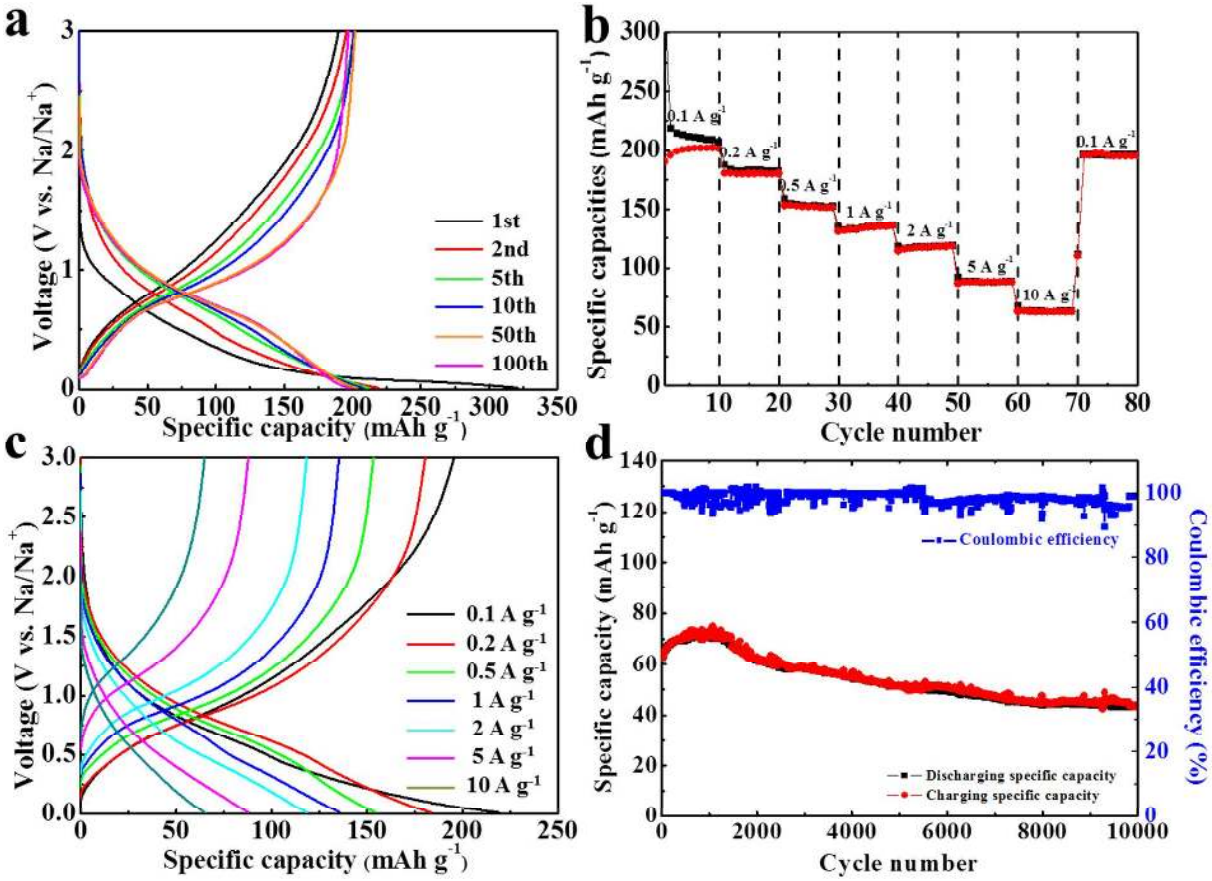

Figure 5. Electrochemical performances of the single-layered 2D ordered mesoporous TiO_2 nanosheets as sodium-ion battery. **(a)** Charge/discharge curves at current density of 0.1 A g^{-1}; **(b)** Cycling performance at various current densities and **(c)** Corresponding selected potential profiles at 0.1 A g^{-1} (1^{st} to 10^{th} cycle), 0.2 A g^{-1} (11^{th} to 20^{th} cycle), 0.5 A g^{-1} (21^{th} to 30^{th} cycle), 1 A g^{-1} (31^{th} to 40^{th} cycle), 2 A g^{-1} (41^{th} to 50^{th} cycle), 5 A g^{-1} (51^{th} to 60^{th} cycle), 10 A g^{-1} (61^{th} to 70^{th} cycle). **(d)** Long-term cycling performance at an ultrahigh current density of 10 A g^{-1}.

TOC Graphic

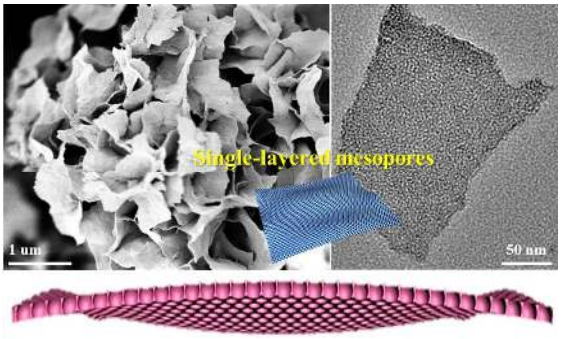

Uniform Ordered Two-Dimensional Mesoporous TiO2 Nanosheets from Hydrothermal-Induced Solvent-Confined Monomicelle Assembly

Kun Lan, Liu Yao, Wei Zhang, Yong Liu, Ahmed Elzatahry, Ruicong Wang, Yongyao Xia, Daifallah Al-Dhayan, Nanfeng Zheng, and Dongyuan Zhao

J. Am. Chem. Soc., **Just Accepted Manuscript** • DOI: 10.1021/jacs.8b00909 • Publication Date (Web): 05 Mar 2018